https://doi.org/10.1038/s44328-025-00030-5

Incubator-integrated electrochemical analysis platform for cell-based studies

Fatma Kurul[1], Meryem Beyza Avci[1], H. Bertan Acar[1], Seda Nur Topkaya[2] & Arif E. Cetin[1,3] ✉

Electrochemical analysis methods are critical for probing cellular behavior, offering sensitivity and versatility. However, challenges such as maintaining in-vivo-like conditions during electrochemical testing can affect data accuracy. To address this, we developed an incubator-integrated electrochemical analysis platform that bridges the gap between cell culture and testing environments, preserving physiological conditions. The platform integrates a microfluidic module for cell-electrode interactions, an incubator module for controlled culture and measurement environments, and a measurement module comprising a screen-printed electrode (SPE) and potentiostat for real-time monitoring. Additionally, the sample preparation apparatus ensures robust cell adhesion and mitigates surface degradation during incubation, enabling consistent and reliable measurements. Through extensive studies with cells, we demonstrated the platform's capability to distinguish varying cell densities and accurately evaluate cell proliferation. Studies on standard-of-care drugs further showcased the platform's utility in assessing drug efficacy, emphasizing its potential for drug screening and personalized medicine applications.

Electrochemical methods emerged as a highly favored analytical tool thanks to their numerous advantages such as rapid response time, cost-effectiveness, high sensitivity, and selectivity[1–3]. Instruments based on electrochemical analyses convert chemical signals into an electrical output[4]. They commonly utilize amperometric, voltammetric, potentiometric, or impedimetric methods to detect the presence of targeted biological or chemical molecules[5]. Electrochemical methods typically involve an electrolytic solution containing the analytes and a three-electrode configuration comprising a working electrode (WE), a reference electrode (RE), and a counter electrode (CE). These electrodes act as transducers by converting chemical signals into electrical outputs, facilitating the analysis of electrochemical processes.[6]. WEs are polarizable electrodes with potentials that vary based on the concentration of the analyte of interest. Among the commonly used WEs are made of platinum, gold, or carbon. CEs allow the passage of current from the solution to WEs, completing the three-electrode configuration. RE provides a stable, constant potential reference point used to control and measure the potential at WE. Popular choices for REs include Ag/Ag+, Ag/AgCl, and saturated calomel electrodes. Recently, advancements in screen printing technology have given rise to screen-printed electrodes (SPEs) which encompass the three electrodes in a compact unit[7–9]. SPEs have gained significant popularity in electrochemical analyses due to their ease of use and suitability for miniaturization[10]. These disposable and compact electrodes are known for their portability and versatility, making them ideal for a variety of applications. The incorporation of SPEs into electrochemical analyses has resulted in the development of integrated systems that have successfully commercialized and provide, rapid, selective, and accurate analytical tools[11,12]. Electrochemical methods have become increasingly prevalent in numerous areas, including environmental[13,14] and food analysis[15–17], medical diagnostics[18,19], pharmaceutical analysis[20], waste management, cellular analysis, and agriculture[21]. In the realm of electrochemical measurements, potentiometry, amperometry, cyclic voltammetry (CV), differential pulse voltammetry (DPV), square wave voltammetry (SWV), and electrochemical impedance spectroscopy (EIS) techniques are frequently employed. These techniques involve the direct transfer of electrons and are based on the measurement of electron transfer resistance. They are designed for the measurement of electrical signals, including current, resistance, or potential.

Due to their sensitive nature, electrochemical methods have been lately utilized for cellular analyses[22]. In literature, the studies based on these analyses either aim to detect the presence of the biomarkers secreted from the cells or to determine cellular properties through direct contact with SPE and cells[23]. As an example of indirect measurement, where the cells are not in contact with the SPE surface, Rojas et al. developed an electrochemical sensor platform for Parkinson's disease. In this platform, they created a Prussian Blue layer electrodeposited on SPEs via drop-casting. This modification was utilized for direct enzyme-free hydrogen peroxide (H_2O_2)

[1]Izmir Biomedicine and Genome Center, Balcova, Izmir, 35340, Turkey. [2]Department of Analytical Chemistry, Faculty of Pharmacy, Izmir Katip Celebi University, Cigli, Izmir, 35620, Turkey. [3]Izmir International Biomedicine and Genome Institute, Dokuz Eylul University, Balcova, Izmir, 35340, Turkey.
✉e-mail: arifengin.cetin@ibg.edu.tr

monitoring in 6-hidroxidopamine cellular model of Parkinson's disease yielding an enhanced sensitivity, e.g., 0.66 $A{\cdot}M^{-1}cm^{-2}$ (ref. 22). Abdelaziz et al. developed an electrochemical method to detect exosomal RNAs isolated from breast adenocarcinoma (MCF-7) and doxorubicin-resistant MCF-7 (MCF-7/ADR) cell lines. Employing gold SPEs in CV, SWV, DPV, and normal pulse voltammetry (NPV) techniques, they were able to distinguish MCF-7 and MCF-7/ADR cells with high accuracy based on exosomal RNA within the concentration range of 0 to 20 ng/μL[24]. On the other hand, as an example of direct measurement, Damiati et al. developed a biosensor system featuring a flow-cell with disposable electrochemical electrodes for detecting Hepatic Oval Cells (HOCs). The system employs an SPE that was enhanced with a multiwall carbon nanotube coated with chitosan and functionalized with specific antibodies. Employing CV and SWV, the sensor confirms electrode functionalization, and the biosensor demonstrates high sensitivity and specificity, providing clear voltammetric peaks at low cell concentrations, which makes it a promising alternative to traditional diagnostic techniques for clinical and oncological applications[25]. As another example, Ding et al. developed a disposable cell impedance sensor, where the cells were in contact with SPEs to track their adhesion and proliferation. They employed polyaniline-modified SPEs to analyze K562 leukemia cells. The addition of polyaniline on the SPE surface promoted cell immobilization and electron transport, yielding a limit-of-detection, e.g., 8.32×10^3 cells/mL[26]. Guohua et al. created a novel cell-based sensor for small-cell lung cancer (SCLC) using lung adenocarcinoma cells (LTEP-P) and their cisplatin-resistant variants (LTEP-P/DDP-1.0), which were cultured on SPEs. Their setup utilizes electrical cell-substrate impedance sensing to measure changes in the electrical impedance response to the chemotherapy drugs, including cisplatin, ifosfamide, gemcitabine, paclitaxel, docetaxel, vinorelbine, etoposide, camptothecin, and topotecan, that promote cell apoptosis. This study enhances the understanding of SCLC treatments and aids in the screening of second-line chemotherapy drugs for personalized cancer treatment[27].

Despite this extensive scope of the electrochemical methods in cell-based studies, a significant deficiency is conspicuous in the literature. In these studies, cells are extracted from the controlled incubator settings, e.g., 37 °C and 5% CO_2, and tested under conditions different from their culture environment, e.g., lower temperature and different pH due to a different CO_2 level, which may exert stress on cells[28]. Changes in cell behavior or proliferation resulting from these external factors undermine the accuracy of cell-based tests[29,30]. Furthermore, seeding cells on the SPE surface in an unsuitable culture environment necessitates locating SPEs in a commercial CO_2 incubator for a finite period of time. This could pose another problem of deterioration of the surface properties of SPE.

In this article, in order to address these problems, we introduced an Incubator-Integrated Electrochemical Analysis Platform to improve the accuracy of electrochemical tests by minimizing the influence of external conditions on cells. The developed electrochemical analysis platform mitigates the effects of exogenous factors such as pH and temperature on live cells incubated on the electrode surface and ensures the continuity of cell viability and proliferation by providing incubator conditions and cell media. Thus, the platform enables high-precision cell-based electrochemical measurements with a heightened degree of accuracy. Figure 1A, B display the schematic illustration and the photograph of the incubator-integrated electrochemical analysis platform.

The platform consists of four main modules:

i. Microfluidic module: Comprising a flow-cell where SPEs interact with cells and measurement solutions and a pump-manifold configuration directing these solutions to the flow-cell.
ii. Incubator module: Comprising two boxes to independently create an incubator environment, e.g., a solution box designed for cell media and measurement solutions and a test box designed for cells seeded on the SPE surface.
iii. Measurement module: Consisting of an SPE and a potentiostat for electrochemical measurements.
iv. Software module: Consisting of a graphical user interface (GUI) that controls the system hardware, and allows conducting electrochemical measurements and data processing on the same panel.

While these modules work together as an integrated system, each serves a specific purpose. The microfluidic module ensures precise liquid handling, the incubator module maintains optimal environmental conditions for cell culture, and the measurement module captures real-time electrochemical data from the SPE. Although some components, such as the flow-cell, appear across multiple modules, this reflects their multifunctional role in supporting each module's unique function rather than indicating redundancy. For example, the flow-cell interfaces with the microfluidic module for liquid delivery, the incubator module for environmental control, and the measurement module for electrochemical testing. This modular yet collaborative design enables seamless functionality and adaptability for diverse experimental setups. In addition to these four modules, we also developed a sample preparation apparatus that allows the incubation of cells on the electrode surface inside a commercial incubator, while preventing the medium level that is necessary for cell adhesion and proliferation from decreasing due to the internal temperature as well as eliminating the corrugation of the SPE surface due to humidity.

The platform operates based on the simultaneous integration of these four modules. The software module transmits all commands related to the hardware modules in the system without the need for commercial software. Initially, cells are incubated on the electrode surface within a commercial incubator for the desired duration using the sample preparation apparatus, which ensures the adhesion of cells onto the electrode surface. Figure 1C shows the schematic illustration of cells adhering on the surface of the three-electrode configuration in SPE. Figure 1D shows the confocal laser scanning microscopy image of phalloidin and DAPI (4',6-diamidino-2-phenylindole) stained MCF-7 cells adhered on the SPE surface after a 24-h incubation. In the figure, the blue staining DAPI highlights the nucleus, while the red staining phalloidin stands for F-actin, demonstrating the strong adhesion and organization of MCF-7 cells on the SPE surface. Figure 1E shows a single MCF-7 cell attaching to the electrode surface, demonstrating that the surface morphology of the three-electrode configuration promotes cell adhesion. The sample preparation apparatus exposes only the three-electrode configuration to the external incubator environment and completely covers the remaining SPE surface while maintaining the cell medium on the SPE surface necessary for cell proliferation. This way, only the surface covered with cells under electrochemical tests is exposed to the incubator environment, preventing its potential effects on the electrical regions of the SPE. Before conducting electrochemical tests with the platform, GUI activates the incubator module, reaching optimal conditions (e.g., 37.0 °C and 5% CO_2) necessary for the cells. Subsequently, SPE that is removed from the sample preparation apparatus is inserted into the flow-cell, ensuring a leak-proof flow, which is then placed inside the incubator box. The SPE is connected to the potentiostat via a connector, where the connections for the three-electrode configuration remain outside the incubator box, preventing the electrical connections from being affected by the incubator environment. Cell and measurement solutions are delivered to the SPE surface through the piezoelectric pumps in the microfluidic module. Before each test, the operator could activate the electrodes via a pre-treatment option. The operator is able to perform tests by selecting the appropriate measurement techniques in the GUI, where the raw data and graphs can be saved afterward. After the measurements are completed, the pumps are used to deliver buffer solutions to the flow-cell to ensure the cleaning of all surfaces in contact with the solutions.

In order to highlight the advantages of the use of our technology in electrochemical analyses, we conducted a comprehensive evaluation utilizing EIS, CV, and DPV techniques on MCF-7 cells. Our results demonstrate the platform's ability to precisely distinguish between different cell densities, a crucial feature for studying cell proliferation dynamics over time. To further showcase the versatility and effectiveness of our technology, we conducted extensive studies on the anti-tumor effects of paclitaxel (PTX), a

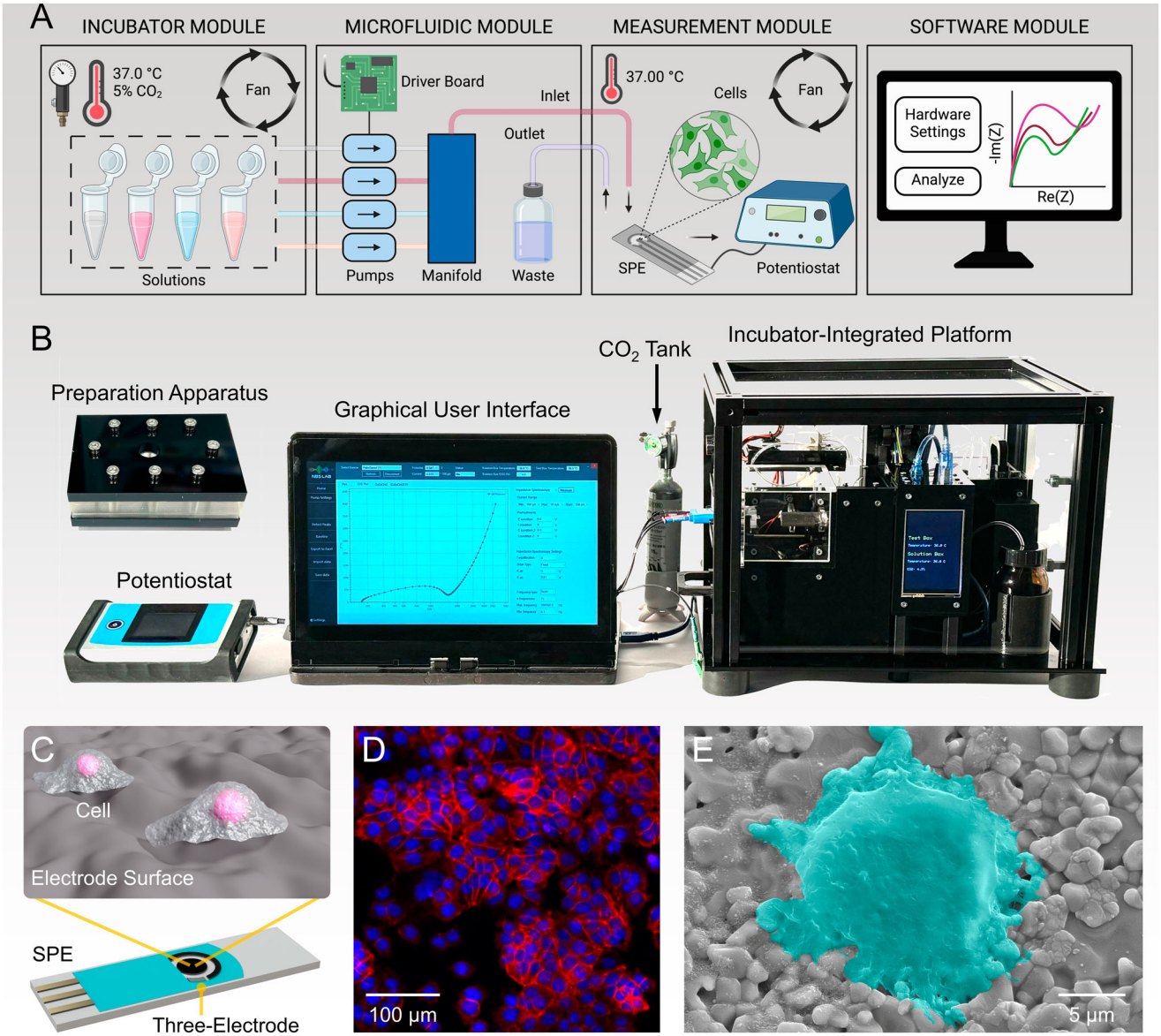

Fig. 1 | Incubator-integrated electrochemical analysis platform. A The schematic illustration and **B** the photograph of the incubator-integrated electrochemical analysis platform and the sample preparation apparatus. Created with BioRender.com. **C** The schematic illustration of cells adhering on the surface of the three-electrode configuration in SPE. Created with SolidWorks Visualize. **D** Confocal laser scanning microscopy image of phalloidin and DAPI stained MCF-7 cells after a 24-h long incubation on the SPE surface with an initial cell density of 2.5×10^5 cells/mL. **E** False-colored (cyan) SEM image of an MCF-7 cell adhered to the electrode surface. Created with Adobe Creative Cloud.

standard-of-care (SOC) drug for cancer treatment. Through electrochemical methodologies, our platform accurately assessed the gradual decrease in cell numbers with increasing PTX concentration, providing valuable insights into drug efficacy. Additionally, we evaluated the usability and functionality of our sample preparation apparatus, crucial for robust cell adhesion, particularly in studies involving adherent cell models. Our findings underscore the platform's capability to elucidate the biophysical properties and therapeutic profiles of cancer cells, offering promising avenues for drug screening and personalized medicine approaches.

Results

Microfluidic module

Microfluidic module consists of two primary components: (i) a flow-cell and (ii) a pump-manifold configuration. Figure 2A illustrates the structure of the flow-cell, comprising two resin-based locking caps and two polydimethylsiloxane-based sealing layers (PDMS, Dowsil SYLGARD™). The resin-based (Formlabs©) molds were used to manufacture the PDMS layers, and the caps were produced using stereolithography (SLA)-based 3D-printing. Supplementary Fig. 1A shows the photographs of the molds and the corresponding PDMS layers. SPE contains the three-electrode configuration with a circular shape in the middle. For that reason, the top PDMS layer has a circular chamber aligned with the area composed of the three electrodes. The bottom PDMS layer has a rectangular space where the SPE is positioned. SPE is then sandwiched between these two PDMS layers, and this assembly is inserted between the two resin-based caps, which serve as a locking mechanism through the use of screws and nuts on each side. Supplementary Fig. 1B, 1C, and 1D show the photographs of the PDMS sandwich, the resin-based caps, and the flow-cell with an inserted SPE within, respectively. The PDMS layers, produced with a high thickness, ensure impermeability by sealing through a compression process with caps. Thanks to their deformation properties, these layers prevent the breakage of the SPE during the compression. Supplementary Fig. 2A, B show the photographs demonstrating the integration of the flow-cell to the test box in the incubator module. Figure 2B shows the complete flow-cell with inlet and

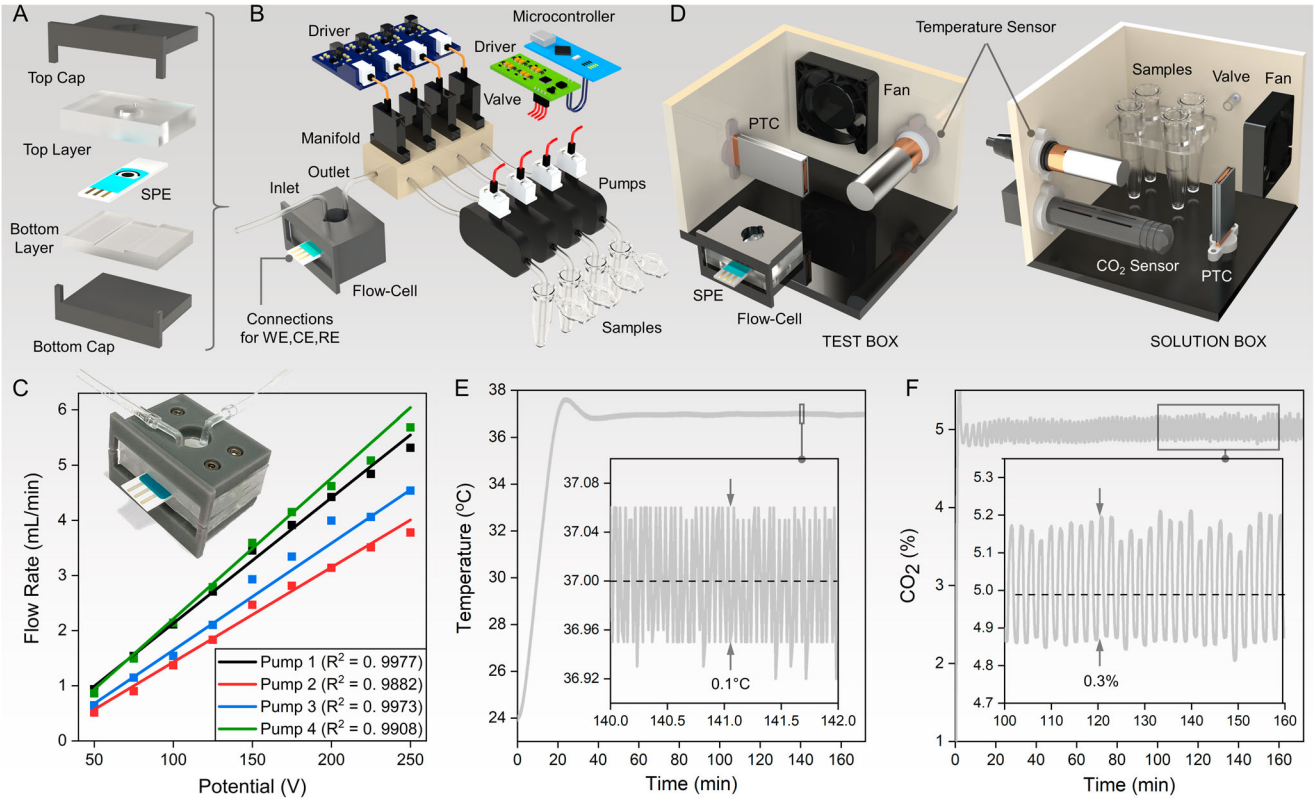

Fig. 2 | Microfluidic and incubator modules. A The schematic illustration of the flow-cell components. Created with SolidWorks Visualize. **B** The schematic illustration of the components of the pump-manifold configuration. Created with SolidWorks Visualize. **C** Calibration of four pumps employed in the microfluidic module. Linear regressions were fitted on the flow rate vs. applied potential data, where squares are the mean values determined from three independent experiments. Figure inset: Photograph of the flow-cell, where an SPE is inserted. **D** Schematic illustrations of the components of the incubator module: Test box and solution box. Created with SolidWorks Visualize. Maintaining **E** temperature and **F** CO_2 concentration at the desired values, e.g., 37 °C and 5%, for the test and solution boxes with the use of the PID controller. Figure insets show the zoomed data, where the temperature and CO_2 values are displayed for the time windows highlighted with black boxes.

outlet allowing the liquid flow over the three electrodes, where the connections for WE, CE, and RE are open. SPE is then connected to the potentiostat via a connector attached to the SPE connections. As shown in Supplementary Fig. 2A, within the system casing, there is a gap to allow the connector to be attached to the SPE in a way that prevents any leakage from the external environment. Inside the test box, there is a space where the SPE is positioned, i.e., the connection points of the SPE remain outside the test box, ensuring that the electrical connections are not exposed to the incubator environment.

Figure 2B also shows the schematic illustration of the pump-manifold configuration, consisting of four piezoelectric pumps (Bartels Mikrotechnik GmbH). Supplementary Fig. 3 shows the photograph of the complete setup of the pump-manifold configuration. To deliver one of the four solutions to the SPE, we developed a 4-input-1-output manifold with four integrated solenoid valves (Takasago Electric Inc.). Each solenoid valve is equipped with a driver to regulate the source current to 250 mA. Valve drivers are controlled with a quadruple relay. The pumps are connected to the pump driver, which is responsible for controlling the power supply for each pump within the range of +1 to +240 V. By adjusting the supply voltage, we can achieve varying flow rates specific to different solutions, such as DI-water, RPMI or PBS. To maintain the linear relationship between voltage and flow rate, the piezoelectric pumps were operated at a frequency of 100 Hz, preventing any disruptions due to the changes in frequency. The pump system is controlled using a microcontroller (Arduino) through the I2C serial communication protocol, while the valves are controlled through the digital pins of the microcontroller. Calibration tests were carried out using solutions including DI-water, RPMI, and PBS, to establish the relationship between input voltage and flow rate. Flow rate was measured for nine different voltages, e.g., 50, 75, 100, 125, 150, 175, 200, 225, 240 V, applied over a period of 60 s for three times, and the mean values were recorded. To determine the mass of solutions dispensed by the pump in a specific duration, a precision balance was used. The flow rate of the piezo pumps was calculated using the formula, e.g., *Flow Rate [mL/min] = Mass [g]/(Density [g/mL] × Time [min])*. As shown in Fig. 2C, flow rate increases with supply voltage, where linear regressions were applied to the experimental data, yielding near unity R^2 for each pump. For four pumps, the maximum deviation from the desired flow rate was determined as low as 2.5%. This level of variability is attributed to the inherent manufacturing tolerances of the piezoelectric pumps, which can result in slight differences in performance despite identical construction.

Incubator module

The incubator module is divided into two compartments, e.g., (i) a solution box and (ii) a test box. Figure 2D shows the schematic illustration of these components, and Supplementary Fig. 4A shows the photograph of the incubator module. Supplementary Fig. 4B shows the photograph of the solution box. The solution box is equipped with a positive temperature coefficient (PTC) heater to uphold the solutions' temperature. To ensure an even distribution of air heated by PTC, a fan is incorporated into the box. For pH control of the cell media, CO_2 gas is employed. The gas is released intermittently from a dual-regulated gas tank, and a solenoid valve maintains controlled gas flow in the solution box. Temperature and CO_2 values are continuously monitored by temperature and CO_2 sensors to sustain constancy at the desired parameters. All components within this box are governed by a microcontroller that features a feedback mechanism to uphold the parameters at the desired values. Supplementary Fig. 4C shows

the photograph of the test box. As the pH of the cell media injected from the solution box is already controlled within the solution box, and cells seeded on the SPE surface are positioned within the flow-cell blocking their contact with the internal environment of the test box, no infrastructure is required for maintaining CO_2 within the test box. Therefore, only temperature is controlled in the test box, and this control is ensured with the use of a PTC, a fan, and a temperature sensor. In addition, incubator parameters for solution and test boxes are displayed on an LCD screen as shown in Supplementary Fig. 4D. In order to ensure the precise stabilization of the desired incubator parameters for the test and solution boxes, they were designed and manufactured to occupy the smallest possible volume. By enclosing all hardware components within an outer casing, the solution and test boxes are further isolated from the external environment, thereby facilitating the control of the incubator parameters.

In order to maintain the temperature of the test and solution boxes at 37 °C, and the CO_2 concentration in the solution box at 50,000 ppm (e.g., 5%), we employed a proportional-integral-derivative (PID) controller[31]. The PID controller of the solution and test boxes represents a comprehensive control system and focuses on the regulation of a defined setpoint temperature, e.g., 37 °C. The algorithm continuously acquires temperature data from the temperature sensor, using this data as input for the PID controller. The PID controller, in turn, adjusts the voltage level of the PTC heater through the pulse-width modulation (PWM) signals to maintain a predefined temperature setpoint. The output of the PID controller corresponds to the PWM value used for temperature control. In the configuration of the PID controller, we engineered a feedback loop integrating the PTC heater with the temperature sensor, governed by the microcontroller. This system was modeled as first-order, e.g., such a system, central to control theory, is described by a first-order differential equation defining the interplay between the system's input and output. This methodology captures the essence of the system's reaction to input variations, focusing solely on the primary derivative of the output in relation to time and excluding considerations for higher-order derivatives. Within this framework of our PID controller, the Proportional, Integral, and Derivative components each undertake unique mathematical operations on the error signal, denoted as $e(t)$, thereby influencing the controller's output. We modeled our PID controller with the following formula, which in turn modulates the controller's output. The schematic illustration of the first-order system, modeling the PID controller designed for the temperature is shown in Supplementary Fig. 5A, and the model for our PID controller is governed by the Eq. 1[31]:

$$u(t) = K_p e(t) + K_i \int_0^t e(t)dt + K_d \frac{\partial e(t)}{\partial t} \quad (1)$$

In this model, K_p represents the Proportional component, which generates an output that is directly proportional to the error's present magnitude. The Integral component, K_i, integrates the error over time, thereby ensuring the system's accuracy over long durations by considering both the magnitude and the persistence of the error. Conversely, the derivative component, K_d, analyzes the error's rate of change, thereby enabling predictions of future deviations based on the current data. Together, these components synergize to adjust the system's control mechanisms, ensuring error mitigation and maintaining system stability for consistent temperature control.

To implement a PID controller within the SPE Incubator system, it is imperative to first establish a model of the system. Given that the system temperature is modeled as a first-order system, deriving this model involves studying the system's transient response. This method focuses on observing and analyzing how the system reacts to changes over time, specifically looking at how it initially responds to input signals and eventually settles to a steady-state. Through this analysis, the dynamic characteristics of the temperature, including its time constant and steady-state gain, can be accurately captured. Such information is crucial for tuning the PID controller parameters, e.g., Proportional (P), Integral (I), and Derivative (D), to achieve optimal control performance, ensuring the system responds efficiently and accurately to setpoint changes or external disturbances. When input is introduced to a control system, its output doesn't stabilize immediately. Instead, it undergoes a period of adjustment, during which the output is considered to be in a transient state. This phase lasts until the system output reaches equilibrium or a steady-state. Therefore, the transient response of the control system is defined as its behavior or reaction during this transient condition. This response is crucial for understanding how the system adapts to changes and for adjusting control parameters to minimize the time it takes for the system to stabilize, thereby improving the overall performance and efficiency of the control system. The transfer function, $G(s)$ in the Laplace domain, of a first-order system can be derived using Eq. 2[32]:

$$G(s) = \frac{K}{s + \frac{1}{\tau}} \quad (2)$$

where K is the system's steady-state gain, τ denotes the system's time constant and s is the complex frequency variable used in Laplace transforms. This transfer function characterizes how the system responds to an input signal, encapsulating both the speed of response, as indicated by the time constant, and the magnitude of the response through the gain. τ gives an indication of how quickly the system responds to changes in input, while K provides a measure of the output amplitude in response to a steady input signal.

For first-order systems, τ plays a crucial role in understanding the system's dynamics, especially in the transient state. It's generally accepted that the system requires approximately 5τ to reach or approach its steady-state after an input disturbance. This timeframe is considered sufficient for the system's output to settle within a small percentage of its final steady-state value. To effectively analyze the transient behavior of the system, it is necessary to apply a step input. A step input is characterized by a sudden change from zero to a specific finite value at time $t = 0$. This abrupt change allows for the observation of the system's response dynamics, including its rise time, settling time, and any overshoot. By examining how the system responds to such an input, one can derive important characteristics like the time constant and the steady-state gain, which are essential for designing and tuning controllers, such as PID controllers, to achieve desired performance criteria.

Supplementary Fig. 5B shows the step response of the incubator system. Based on the step response, the system stabilized at a final temperature of 48.35 °C after 2480 s, corresponding to 5τ, e.g., τ is calculated as 496 s, which means that within 496 s after the step input is applied, the system's temperature should reach approximately 63.2% of its final value, assuming no oscillations. This is a critical point in understanding and predicting the system's behavior under various input conditions. Figure 2E shows the real-time temperature data for a 170-min period. As shown in the figure, the desired temperature value is achieved within 30 min, and precisely maintained for long durations. In the figure inset, we show the temperature values for a shorter time window, e.g., 2 min, demonstrating that the temperature of the test and solution boxes was stabilized around 37 °C with a variation of only 0.1 °C.

To regulate the CO_2 concentration in the solution box, the CO_2 sensor continuously measures the concentration value, which is then fed into the PID algorithm. Control of the concentration is accomplished by manipulating the opening and closing of the solenoid valve connected to the CO_2 tube within the solution box. The algorithm employs a series of conditional statements with different delay settings for diverse concentration ranges and opens or closes the solenoid valve. The PID controller calculates the duration for which the solenoid valve needs to remain open to bridge the gap between the desired and current concentration values. As long as the solenoid valve is open, CO_2 is introduced inside the CO_2 tank, and the valve is closed when the concentration reaches 50,000 ppm. To configure the PID controller, we employed Ziegler-Nichols tuning method[33]. This method entails observing the system's reaction to perturbations and determining the critical parameters such as the ultimate gain and the oscillation period.

Based on these parameters, we derived the proportional, integral, and derivative gains for the controller. These preliminary settings serve as a foundation for further refinement, aiming to enhance the controller's ability to regulate the system effectively. The Ziegler-Nichols approach provides reliable solutions for developing robust control strategies. The critical asset, referred to as the Sweet Spot, is identified by the onset of steady oscillation, denoted as the ultimate gain, K_c, and the oscillation period P_c. Subsequently, the PID controller's key settings, e.g., proportional, integral and derivative gains, are calculated using, $K_p = 0.6K_c$, $K_i = 2K_p dt/P_c$ and $K_d = K_p P_c/8dt$ where dt represents the time step. These calculated coefficients are then implemented in the PID controller to evaluate its performance in system regulation. Continuous observation and adjustment of these coefficients are necessary to optimize control. Ultimately, the Ziegler-Nichols method provides an effective starting point for the calibration of PID coefficients. This method facilitates initial tuning, which is then refined through trial and error to achieve optimal system performance. Figure 2F shows the real-time CO_2 concentration data for a 170-min period, where the system reaches the desired concentration within the first 5 min. As shown in the figure inset, demonstrating a 60-min window, CO_2 concentration was maintained at 5% with only 0.3% variation.

Measurement module

Measurement module consists of an SPE, a potentiostat, and a connector that facilitates their interconnection. The developed analysis platform can be integrated to any commercial potentiostat, and the software module can recognize different software programs specific to potentiostat manufacturers. For our demonstration regarding the functionality of our technology, we employed PalmSens4, a USB and battery powered potentiostat. The potentiostat operates by controlling the potential difference between a working and a reference electrode through the application of current via a counter electrode in a classical three-electrode setup.

In order to underscore the advantages of employing our electrochemical analysis platform for cellular applications, we conducted EIS, CV, and DPV studies utilizing MCF-7 cells. EIS serves as a critical technique for investigating the electrical characteristics of systems, particularly in the context of biosensors and various electrochemical devices[34–36]. EIS involves the application of a small amplitude AC voltage (alternating current) to the system, with subsequent measurement of the resulting current response[37]. EIS utilizes a transfer function methodology to simulate the response of the output signal (alternating current or voltage) concerning the input signal (alternating voltage or current) across a broad spectrum of frequencies. The following impedance analysis spans a spectrum of frequencies, and this impedance is represented as a complex number encompassing real (resistive) and imaginary (reactive) components. The assessment of live biological cells through impedance measurement stands as a widely embraced approach due to its label-free nature, non-invasive characteristics, and quantitative analytical capabilities for gauging cell conditions. This technique is acknowledged for its user-friendly nature and adaptability in device design and manufacturing processes. Designing a sensor for measuring cell impedance relies on two key factors, e.g., electrodes for applying an electric field to the cell-medium system and a device for integrating these electrodes with the liquid delivery system. Through the analysis of impedance data collected across varying frequencies, valuable insights into the electrical characteristics of the material or system being studied could be gained, encompassing parameters such as electrical conductivity, dielectric properties, capacitance, and phenomena associated with interfaces.

CV stands as a technique for probing the electrochemical characteristics of systems, especially in applications such as biosensors and various electrochemical devices[38]. CV technique is utilized to analyze the reduction and oxidation processes of molecular species[39]. In CV, a triangular waveform is applied as a scanning potential for WE to detect the generated current. The resulting voltammogram, a graph of current plotted against applied potential, yields crucial insights into the reaction mechanism, including redox potential, reversibility, reaction rate, and analyte concentration[40]. Differential pulse voltammetry (DPV) emerges as a crucial technique for exploring the electrochemical characteristics of systems, particularly in the realm of biosensors and various electrochemical devices[41]. DPV involves the application of discrete pulses of potential to the system, with subsequent measurement of the resulting current response. Unlike other electrochemical methods, DPV focuses on the dynamic response of the system to these discrete potential pulses, providing valuable information about redox processes[42]. DPV achieves this by applying a series of potential pulses superimposed on a linear potential scan, resulting in an enhanced signal-to-noise ratio and reduced background current. This allows for better detection and quantification of analytes, particularly in complex samples, making DPV a preferred technique for trace analysis and the determination of low concentrations of electroactive species.

Software module

The graphical user interface (GUI) of the platform was developed using Microsoft Visual Studio in C# language. Figure 3 shows the main panel of the GUI, providing the operator with control over the hardware components of the Microfluidic, Incubator, and Measurement modules. The GUI displays a list of connected potentiostats on the top panel (left-hand side, in gray color), showcasing their respective statuses and device specifications, e.g., potential (V) and current (A). For the control of the selected potentiostat, we integrated the open-source PalmSens4 Software Development Kit (SDK) into the GUI for electrochemical analyses. This integration enables the effective control and measurement tools for PalmSens4. The communication protocol employed for the interaction between GUI and PalmSens4 is based on serial communication. Moreover, the top panel (right-hand side, in gray color) provides information regarding the temperature of the solution and test boxes and the CO_2 concentration of the solution box. This functionality facilitates the real-time monitoring of both the potentiostat and the incubator, significantly enhancing the overall management capabilities of the platform.

"Home" menu (on the black panel) enables the operator to conduct a variety of measurements using different techniques, including CV, DPV, and EIS. The operator can choose the desired technique for the electrochemical analyses, and the GUI shows the necessary parameters on the panel on the right-hand side for the selected technique. For this panel, the operator can also perform activation of SPEs with the user-defined parameter values displayed in the "Pretreatments" menu. The table in Supplementary Fig. 6 shows the parameters used for each electrochemical technique. Once these parameters are provided by the operator, the measurement is initiated via "Measure" command. Subsequently, the acquired measurements are visually presented as a 2-dimensional graph, and the resulting data is made available to the operator. For example, in Fig. 3, the GUI represents the result of an EIS measurement, e.g., Real(Z) vs. -Im(Z) graph. On the black panel, "Detect Peaks" command identifies the peaks on the graph derived from the measurement. "Baseline" command draws a baseline on the graph for establishing a reference line. "Export to Excel" command allows the saving of experiment results as an Excel file, "Import Data" command facilitates the loading of previous experiment results into the GUI, and "Save Data" command records the raw measurement data. The "Settings" command (Supplementary Fig. 7) reveals an "Auto Save Settings" menu, facilitating the automatic saving of measurements conducted with the potentiostat. Additionally, there is a "Solution" menu, allowing the recording of the density and the names of the liquids used in pump calibration.

"Plot" command on the top left serves as the graphical representation of the post-measurement data, encompassing measurement results and analytical tools. For example, in the case of an EIS plot, GUI illustrates how impedance varies with frequency during a potentiostatic measurement. Additionally, "DataGrid" and "DataGridEIS" display detailed information about the experiments, presenting parameters such as potential, current, or other relevant data based on the specific experiment settings in DPV or CV, and EIS measurements, respectively.

The microfluidic module is controlled from the "Pump Settings" menu (on the black panel), which allows the calibration of the pumps in a

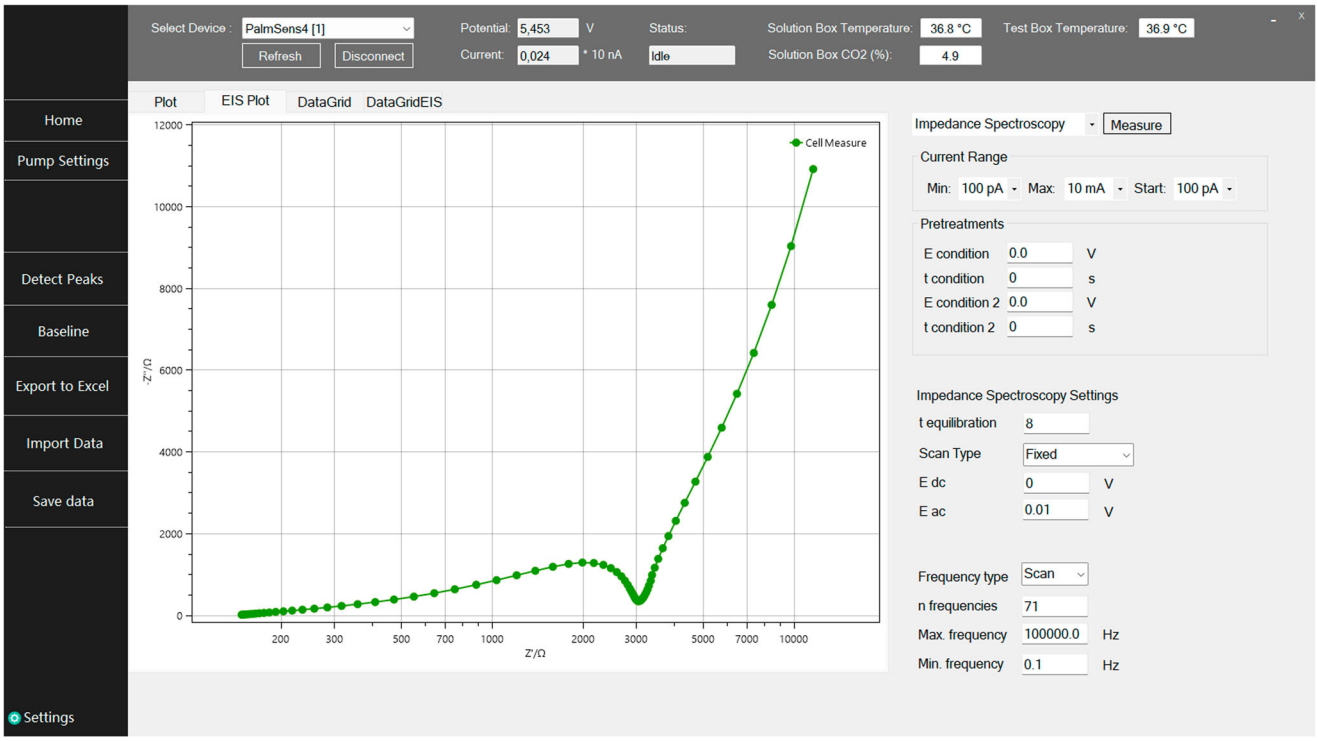

Fig. 3 | The graphical user interface (GUI) of the incubator-integrated electrochemical analysis platform. The figure shows a representative example of EIS measurement results for an SPE seeded with MCF-7 cells at an initial density of 5×10^5 cells/mL.

subpanel. In this subpanel (Supplementary Fig. 8), calibration can be performed for each pump independently via the "Select Pump" menu, where the operator can choose the pump and the calibration solution with its density information. The operator can also determine the number of potentials up to ten potential values between 1 and 240 V and the repetition time of each potential used for the calibration study ("Select Voltage Number" and "Select Set Number"). In "Pump Modes" menu, the operator can manually operate the pumps either for a required volume of solution or with a flow rate for a desired duration. During the electrochemical measurements, the pumps are turned off to eliminate any mechanical or chemical fluctuations that could interfere with the test data, i.e., they are not simultaneously operated with the test execution commands. This menu also allows the operator to prime the pumps after their installation by running them at the maximum potential, e.g., 240 V, and frequency of 100 Hz for a desired duration, which is critical for new pumps or pumps not used for a long period of time to reach their maximum flow efficiency.

Sample preparation apparatus

Ensuring an environment conducive to robust and healthy cell attachment is crucial, directly influencing the reliability of electrochemical results. To address this critical issue, we developed a sample preparation apparatus designed to seed cells onto the SPE surface inside a commercial incubator. This apparatus covers the entire SPE surface, leaving only the three-electrode configuration exposed to the incubator environment. It safeguards the connections on the SPE from potential issues arising due to the humid conditions within the incubator. The illustration in Fig. 4A shows the sample preparation apparatus in use during the incubation phase, where the electrode connections are intentionally isolated and not exposed to external devices like the potentiostat. This design ensures that the SPE connections are safeguarded from potential issues arising from the humid incubator environment, allowing optimal cell adhesion and proliferation. Once the incubation phase is complete, the SPE is carefully removed from the sample preparation apparatus and transferred to the Flow-Cell for electrochemical measurements. In the Flow-Cell setup, the SPE connections are exposed and securely connected to the potentiostat, enabling the performance of EIS, CV, and DPV measurements. This workflow ensures that each module of the platform fulfills its specific role in maintaining cell viability and achieving high-precision electrochemical analyses. The apparatus consists of two PDMS layers, where the top layer features a reservoir (denoted as the sample chamber in Fig. 4B) aligned with the three-electrode configuration of SPE, exposing the surface to the incubator environment. The bottom layer incorporates a rectangular space accommodating the SPE. Supplementary Fig. 9A provides the photograph of the polylactic acid-based molds (PLA, MakerBot Industries, LLC.) manufactured through 3D-printing, which is used to form the PDMS layers. The PDMS layers are enclosed between two acrylic locking caps. As shown in Supplementary Fig. 9B, the top cap possesses a hole aligned with the three-electrode configuration of the SPE and the reservoir in the top PDMS layer. As shown in Fig. 4B—left, the acrylic caps and the PDMS layers are assembled using eight head screws. By tightening the screws and using the deformability of PDMS, the sample preparation apparatus ensures robust sealing for extended durations, lasting for weeks determined through leak experiments performed with food coloring. As shown in Fig. 4C, the operational procedure involves pipetting cells onto the surface of the three-electrode configuration through the circular hole in the top cap and PDMS layer, followed by inserting the sample preparation apparatus into a commercial incubator. This approach simplifies the cell-seeding processes by eliminating the operator-related errors during pipetting by directing the cell medium to the three-electrode configuration and facilitates the subsequent incubation steps while protecting the SPE properties for further cellular analyses.

More importantly, by establishing a volume on the electrode surface, we were able to create an environment for cells similar to a flask or other cell containers designed solely for cell culturing. Figure 4B—right shows the photograph of an SPE, where the surface of the three-electrode configuration is covered with cell medium by pipetting. Incubating cells by directly pipetting them onto the surface of SPE, the dispersion of the cell medium across the SPE surface leads to a minimal height of the liquid medium. This is due to the expansive spread of the medium, facilitating a broader contact area, inadvertently accelerating the rate of evaporation that could diminish the cell medium. Furthermore, by creating a volume with a finite height over

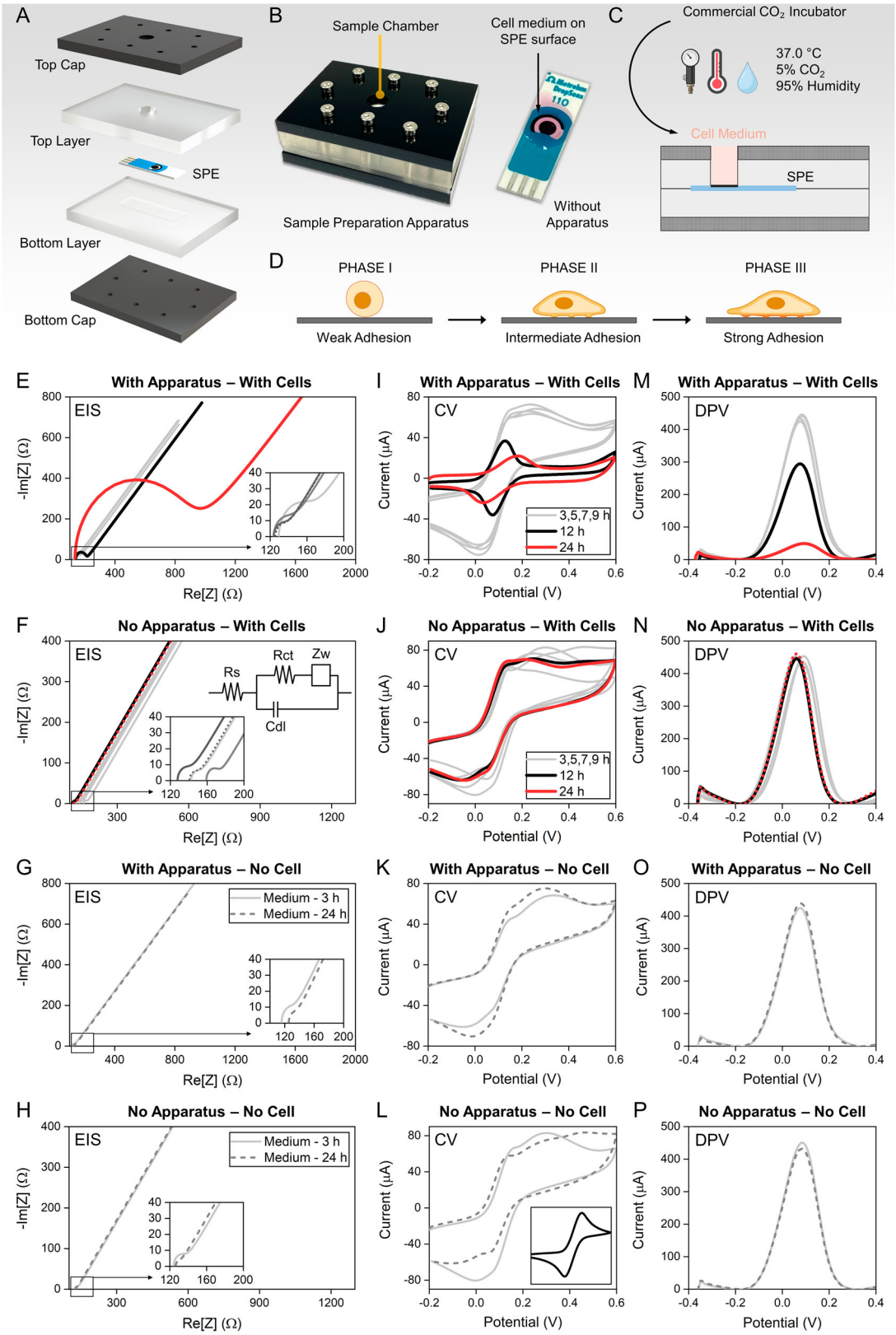

the surface with the use of the sample preparation apparatus, we ensure sufficient nutrients and agents for cell proliferation and the other ingredients that promote cell attachment, while seeding the cells with pipetting leaves a minute amount of cell medium due to the expansion of the medium on the surface.

Sample preparation apparatus promotes cell attachment

To demonstrate the advantageous nature of the sample preparation apparatus in promoting cellular activities in commercial CO_2 incubators, we conducted a comparative study. Here, we compared two systems by performing EIS, CV, and DPV using MCF-7 cells. In this investigation, we

Fig. 4 | Effects of cell adhesion on the electrochemical properties of SPE. A The schematic illustration of the constituting elements of the sample preparation apparatus. Created with SolidWorks Visualize. **B** The photograph of the sample preparation apparatus, where an SPE is inserted between the PDMS layers (left), and the photograph of an SPE, where the surface of the three-electrode configuration is covered by cell medium realized with manual pipetting (right). **C** The schematic illustration of the sample preparation apparatus, where the cells are seeded on the surface of the three-electrode configuration. Created with BioRender.com. The finite height of the sample chamber allows a sufficient volume of cell medium for healthy cell proliferation and adhesion inside the commercial incubator. **D** The schematic illustration of the cell adhesion phases. Created with BioRender.com. **E** EIS, **I** CV, and **M** DPV results for the SPEs located inside a commercial incubator with the use of the sample preparation apparatus, where the electrode surface was seeded with MCF-7 cells of 1×10^5 cells/mL density. **G** EIS, **K** CV, and **O** DPV results for the cell-free SPEs immersed in cell media located inside a commercial incubator with the use of the sample preparation apparatus. **F** EIS, **J** CV, and **N** DPV results for the SPEs located inside a commercial incubator (no sample preparation apparatus), where the electrode surface was seeded with MCF-7 cells of 1×10^5 cells/mL density. **H** EIS, **L** CV, and **P** DPV results for the cell-free SPEs immersed in cell media located inside a commercial incubator (no sample preparation apparatus). Incubation durations after seeding the cells on the surface of the three-electrode configuration: 3, 5, 7, and 9 h (gray), 12 h (black), and 24 h (red). Cell-free SPEs immersed in the cell medium in an incubator environment: 3 (gray) and 24 h (dashed gray). For EIS spectra, figure insets zoom into a small Re[Z] range, displaying the impedance behavior for the incubation durations of 3, 5, 7, and 9 h (with cells), and 3 and 24 h (without cells). Figure 4F-inset shows the equivalent circuit model used to fit the EIS data. Figure 4L-inset displays a typical CV spectrum of the bare SPE.

monitored the electrochemical spectra of the SPE seeded with cells at a density of 1×10^5 cells/mL. The cells were first incubated using the sample preparation apparatus inside a commercial incubator for durations of 3, 5, 7, 9, 12, and 24 h. After incubation, the SPE was transferred to the Flow-Cell setup, where the connections to the potentiostat were securely established. The Flow-Cell, containing the SPE, was then placed inside the test box of the incubator module for electrochemical measurements, ensuring optimal environmental conditions. We then compared the results with a scenario where the sample preparation apparatus was not utilized.

Cell adhesion is a process divided into three distinct phases[43]. Illustrated in Fig. 4D, Phase I involves the initial attachment of cells to the substrate, where integrins form bonds with the extracellular matrix, and the adhesion strength is relatively weak. Transitioning to Phase II, the interaction between integrins and extracellular matrix ligands intensifies, leading to integrin-clustering. Cells enhance the number of surface contact points with the extracellular matrix through actin-containing fibers. During this phase, cells spread on the surface, adopting a flattened shape with a decreased height. The adhesion strength in Phase II is intermediate, falling between weak and strong. Finally, in Phase III, cells establish focal adhesions and actin-containing fibers, which undergo reorganization, redistributing the cytoskeleton. Focal adhesions consist of receptors for extracellular matrix proteins and structural components linking fibers to the extracellular matrix and cell membrane. At this stage, cells achieve maximum spread area, and the adhesion strength becomes strong. The progression of cell adhesion strength increases over time, augmenting the number of bonds formed between receptors and extracellular matrix proteins.

A robust cell adhesion on the electrode surface is critical for the reliability of electrochemical analyses on cells, as it eliminates any loss in the signal due to weak cell attachment. Our investigation focused on assessing the impact of the sample preparation apparatus on the adhesion of cells to the electrode surface, utilizing EIS as our first method of analysis. Figure 4E displays the EIS spectra for various incubation durations, utilizing the sample preparation apparatus for cell culturing in a CO_2 incubator. In practical electrochemical systems, the Nyquist plot pattern typically exhibits both a semicircle and a straight line across a broad frequency spectrum in a faradaic impedance spectrum. The semicircle signifies the region where the electrochemical process is governed by charge transfer phenomena, while the straight line denotes the area where mass transfer phenomena control the electrochemical process. The equivalent circuit is designed to include a representation of cell impedance alongside the impedance of the culture medium, incorporating components such as cell membrane capacitance and cytoplasmic resistance. Figure 4F illustrates our equivalent circuit model used to fit the EIS data, where Rct is the electric charge transfer resistance, Rs the electrolyte resistance, Cdl is the double layer capacitance at the surface of the electrode, and Zw is the Warburg impedance. Cell attachment increases the total mass on the electrode surface. This additional mass, in turn, modulates the mobility of charge carriers (comprising electrons or ions) across the electrode interface, consequently leading to higher resistance. Moreover, cell attachment has effects on the charge transfer kinetics occurring at the electrode interface. This perturbation in the rate of electron transfer holds the potential to exert an influence on the overall impedance characteristics of the system. Figure 4G shows the impedance spectra of the cell-free SPEs incubated in the cell medium for 3 and 24 h with the sample preparation apparatus. Here, SPEs seeded with cells via the sample preparation apparatus, incubated in the commercial incubator for 3, 5, 7, and 9 h (Fig. 4E, gray curves), display a similar behavior with the cell-free SPEs (Fig. 4G) implying weak cell adhesion in these cases. As mentioned above, this is attributed to the insufficient external conditions provided without the sample preparation apparatus, where the liquid medium spreads thinly over the electrode surface, leading to rapid evaporation and a lack of sufficient nutrients and adhesion-promoting factors required for robust cell attachment. The same similarity could be observed from the charge transfer resistance, e.g., Rct = 12.4 Ω (3-h cell-free), 10.3 Ω (24-h cell-free), 14.2 Ω (3-h incubation), 17.3 Ω (5-h incubation), 15.8 Ω (7-h incubation), and 11.8 Ω (9-h incubation). However, a noticeable variation in the EIS spectrum is observed at the 12-h mark (black curve), e.g., Rct = 69.1 Ω. The impedance further increases after an additional 12 h of incubation (*t*: 24 h, red curve), where Rct = 728.3 Ω. Here, longer incubation times leading to more significant impedance changes suggest that the cells are actively interacting with the SPE surface over time, directly related to cell adhesion. Over an extended incubation period, cancer cells have more time to attach, spread, and adhere to the surface of the SPE. The increasing number of attached cells and the spreading of the cell layer contribute to an increase in impedance. For the incubation times 3, 5, 7, and 9 h, cells are in Phase I, where the cell-substrate contact locations are low in number and cell adhesion is weak, i.e., no impedance change was observed for short incubation durations. As cells started to attach on the surface and the number of contact locations increased for Phase II, we observed an increase in the impedance (*t*: 12 h). As in Phase III, cells strongly adhere on the SPE surface, i.e., we observed a dramatic signal increase (*t*: 24 h). On the other hand, in the case of cell seeding without the sample preparation apparatus, cell adhesion is weak even after a 24-h incubation period due to the insufficient external factors required for healthy cell adhesion. For instance, the EIS spectra of the cell-free SPEs (Fig. 4H) are similar to that of the SPEs seeded with cells of different incubation durations (Fig. 4F), supporting our claim that in the absence of the sample preparation apparatus, cell adhesion is either absent or weak. From the charge transfer resistance, a similar behavior could be observed, e.g., Rct = 11.7 Ω (3-h cell-free), 8.3 Ω (24-h cell-free), 9.3 Ω (3-h incubation), 12.8 Ω (5-h incubation), 8.7 Ω (7-h incubation), 12.6 Ω (9-h incubation), 9.3 Ω (12-h incubation), and 10.7 Ω (24-h incubation).

We further investigated the effect of the sample preparation apparatus on cell adhesion on the electrode surface via CV and DPV analyses. Figure 4I, J shows the related CV spectra for different incubation durations with and without the sample preparation apparatus, respectively. (Fig. 4L-inset shows a typical CV behavior of the bare SPE, e.g., no exposure to cellular or any related media). As expected, for the case of the sample preparation apparatus (Fig. 4I), for the incubation times of 3, 5, 7, and 9 h, no further changes occur compared to the CV spectra of the SPEs immersed in cell media for 3 and 24 h (Fig. 4K). Here, for example, the anodic peak current

values were obtained as, e.g., 65.3 μA (3-h cell-free), 75.7 μA (24-h cell-free), 70.3 μA (3-h incubation), 68.8 μA (5-h incubation), 73.1 μA (7-h incubation), and 69.5 μA (9-h incubation). For longer incubation durations (Fig. 4I), the amplitude of the oxidation and reduction peaks decreases, while the positions of the oxidation and reduction peaks further shift, e.g., the anodic peak current is calculated as 36.2 μA for 12-h incubation, and 17.3 μA for 24-h incubation. The observed variations in the peak current signal (the amplitude of the oxidation and reduction peaks) during CV studies suggest alterations in the electrochemical processes influenced by the attachment of cells to the electrode surface. As cells adhere to the electrode surface, these bindings induce modifications in the electrical properties of the system, resulting in a decrease in the peak current signals. The adhered cells introduce an increased mass to the electrode surface, influencing the mobility of charge carriers, including electrons or ions, across the electrode interface, and contributing to changes in the system's resistance. Additionally, the attachment of cells induces shifts in the positions of the oxidation and reduction peaks. These shifts indicate changes in the redox behavior of the electrochemical system and could be attributed to the altered kinetics of the redox reactions, modifications in the local environment at the electrode interface, or variations in the nature of the electroactive species. On the other hand, in the absence of the sample preparation apparatus which yields no or weak cell adhesion, the CV behavior of the SPEs seeded with cells for different incubation durations (Fig. 4J) is similar to that of the cell-free SPEs incubated in the culture environment for 3 and 24 h (Fig. 4L). For instance, the anodic peak current is calculated as 70.1 μA (3-h cell-free), 68.1 μA (24-h cell-free), 68.4 μA (3-h incubation), 66.3 μA (5-h incubation), 65.7 μA (7-h incubation), 69.8 μA (9-h incubation), 68.8 μA (12-h incubation), and 71.9 μA (24-h incubation).

Similarly, in the DPV studies with the use of the sample preparation apparatus, for the incubation times of 3, 5, 7, and 9 h (Fig. 4M), no further changes occur compared to the DPV spectra of the SPEs incubated in cell media for 3 and 24 h (Fig. 4O). The baseline corrected peak current values are determined as, 435.8 μA (3-h cell-free), 446.4 μA (24-h cell-free), 442.3 μA (3-h incubation), 431.7 μA (5-h incubation), 433.1 μA (7-h incubation), and 440.7 μA (9-h incubation). As shown in Fig. 4M, for longer incubation durations, the peak current decreases from 12 h (black curve, 294.1 μA) to 24 h (red curve, 49.4 μA). The observed changes in the peak current signals during DPV studies are indicative of alterations in the electrochemical behavior induced by the binding of cells to the electrode surface. When cells adhere to the three-electrode configuration, this binding results in modifications to the electrical properties of the system, leading to a drop in peak current signals. The adhered cells contribute to an increased mass on the electrode surface, impacting the mobility of charge carriers such as electrons or ions across the electrode interface. This modulation in charge carrier mobility leads to changes in the resistance of the system. Additionally, the attachment of cells influences the charge transfer kinetics at the electrode interface, perturbing the rate of electron transfer and further contributing to the observed variations in the peak current signals. Similarly, in the case of no sample preparation apparatus, the DPV spectrum of the SPEs seeded with cells for different incubation durations (Fig. 4N) is similar to that of the cell-free SPEs incubated for 3 and 24 h (Fig. 4P), e.g., the baseline corrected peak current values are determined as 444.5 μA (3-h cell-free), 436.3 μA (24-h cell-free), 440.1 μA (3-h incubation), 438.1 μA (5-h incubation), 442.7 μA (7-h incubation), 435.3 μA (9-h incubation), 439.8 μA (12-h incubation), and 446.7 μA (24-h incubation).

Electrochemical analysis platform monitors cell proliferation

To demonstrate the capability of our platform to monitor cell growth and proliferation based on cell division (as illustrated in Fig. 5A-top), we investigated the effect of varying cell densities on the electrochemical properties of the SPE. By seeding MCF-7 cells at different densities, we aimed to model and quantify cell growth, as the density directly correlates with the number of cells adhered to the electrode surface. This approach allows us to evaluate how changes in cell coverage impact electrochemical behavior, providing insights into the platform's potential for studying proliferation dynamics. To do so, we seeded MCF-7 cells at different densities, e.g., ranging from 2.5×10^5 cells/mL to 2×10^6 cells/mL for 24 h. Figure 5B shows the variations in EIS, CV, and DPV spectra for different cell densities. In the figures, orange curves denote the electrochemical behavior of the cell-free SPEs incubated for 24 h under a cell medium. In EIS, we observed impedance increases for higher cell densities, which is attributed to the increased cell coverage, in other words, higher confluency. Higher cell densities result in more cells adhering to the electrode surface, leading to increased coverage with non-conductive cell membranes. This increased coverage effectively reduces the area available for electrochemical reactions to occur, thus impeding the mobility of charge carriers and increasing impedance. For example, a meaningful increase in Rct is observed for the cell density of 5×10^5 cells/mL (black curve), e.g., 53.4 Ω, while Rct shows a minor increase, e.g., 16.9 Ω, for 2.5×10^5 cells/mL (gray curve), compared to the SPE response under cell medium (orange curve, Rct = 11.3 Ω). As the surface coverage increases with higher cell densities, we observed a dramatic increase in Rct, e.g., 630 Ω for 7.5×10^5 cells/mL (red curve), 1095 Ω for 1×10^6 cells/mL (blue curve), and 2125 Ω for 2×10^6 cells/mL (green curve).

Our results demonstrate that with the use of CV and DPV, the developed platform could determine the cell coverage on the electrode surface with an ability to differentiate cell densities as low as 2.5×10^5 cells/mL, which could be used to monitor cell proliferation in long-term culture studies. In the CV analyses (Fig. 5C), the peak current signal decreases with cell density. Here, the presence of a higher number of cells on the electrode surface can physically block access to the electrode by electroactive species in the solution. This blockage impedes the efficient transfer of charge carriers between the electrode and the solution, resulting in a decrease in the peak amplitude. In CV, significant decreases were observed for all cell densities compared to the SPE response under cell medium (orange curve, 68.7 μA). For example, the anodic peak current amplitude gradually decreases with cell density, e.g., 55.4 μA for 2.5×10^5 cells/mL (gray curve), 32 μA for 5×10^5 cells/mL (black curve), 24.5 μA for 7.5×10^5 cells/mL (red curve), 12.4 μA for 1×10^6 cells/mL (blue curve), and 7 μA for 2×10^6 cells/mL (green curve). Similarly in DPV (Fig. 5D), the decrease in the peak current signals with cell density can be explained by the reduced electroactive species accessibility, e.g., as the cell density increases, a denser layer of cells forms on the electrode surface, which can physically block the access of electroactive species to the electrode. This decreased accessibility reduces the number of electroactive species available for redox reactions, resulting in a decrease in peak current signals. Furthermore, the presence of a higher number of cells on the electrode surface can increase the charge transfer resistance at the electrode-electrolyte interface. This increased resistance hinders the efficient transfer of charge carriers (such as electrons or ions) between the electrode and the solution, leading to a decrease in the peak current signals. Here, the peak current under cell medium (orange curve, 428.8 μA) gradually decreases with cell density, e.g., 391.6 μA for 2.5×10^5 cells/mL (gray curve), 261.3 μA for 5×10^5 cells/mL (black curve), 48.6 μA for 7.5×10^5 cells/mL (red curve), 30 μA for 1×10^6 cells/mL (blue curve), and 4.4 μA for 2×10^6 cells/mL (green curve).

Electrochemical analysis platform evaluates therapeutic effect of SOC drugs

In order to demonstrate the capability of our electrochemical analysis platform to evaluate the therapeutic effect of the standard-of-care (SOC) drugs, we studied paclitaxel (PTX) with MCF-7 cell line. PTX, a chemotherapy agent widely utilized in treating diverse cancer types, falls under the category of taxanes[44]. Its mechanism of action involves disrupting the normal function of microtubules within cells, integral components of the cellular cytoskeleton that are crucial for cell division. Figure 5A-bottom shows the schematic illustration of the PTX mechanism. PTX achieves its anti-tumor effects through several mechanisms[45–47]. First, it binds to microtubules, promoting their stabilization and interfering with their dynamic behavior during the cell cycle. Second, it inhibits cell division by disrupting the formation of the mitotic spindle, essential for the segregation of chromosomes during mitosis. Third, it induces cell cycle arrest,

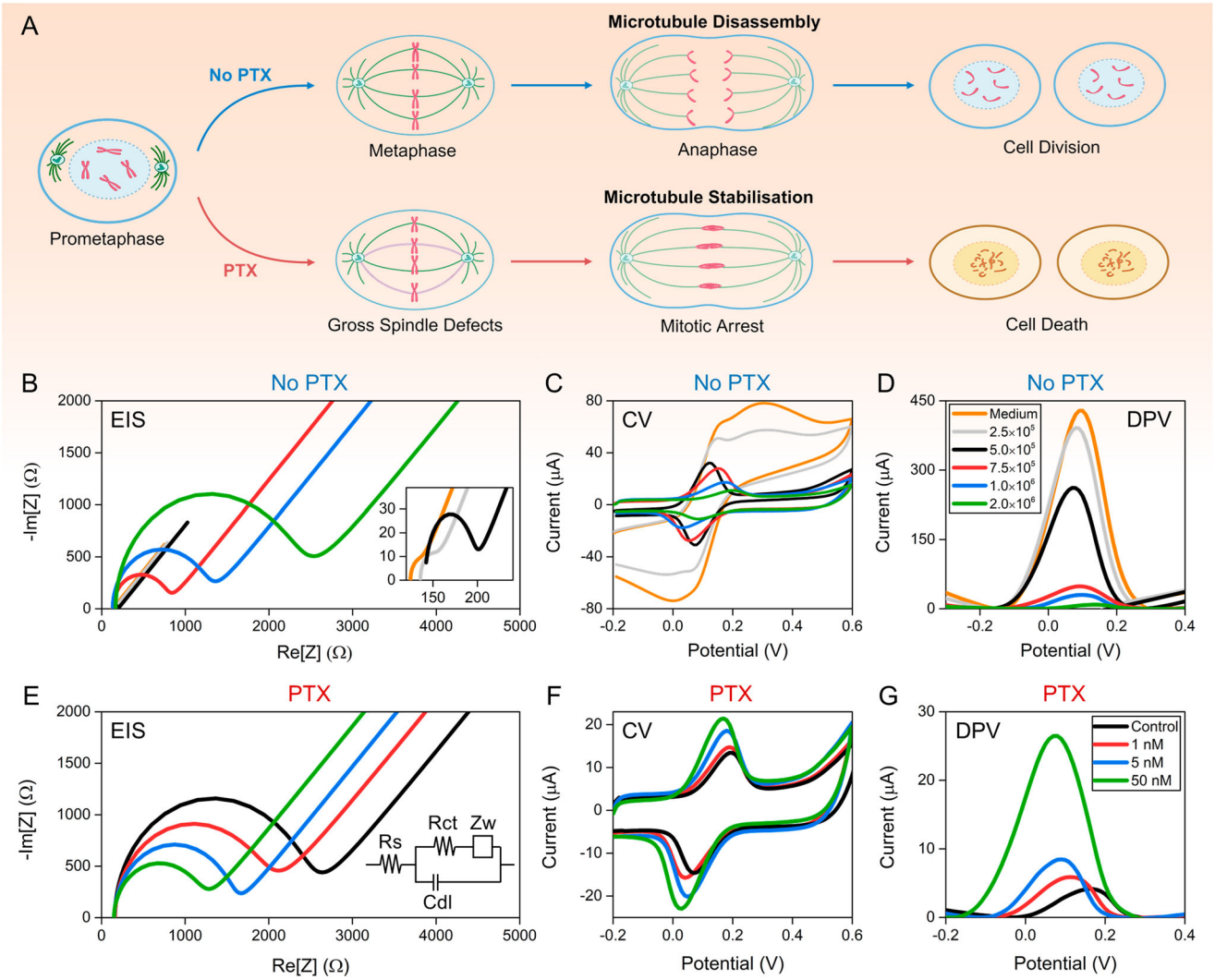

Fig. 5 | Monitoring cell coverage and therapeutic response of MCF-7 cells. A The schematic illustration of the PTX mechanism. Created with BioRender.com. **B** EIS, **C** CV, and **D** DPV results for the SPEs seeded with MCF-7 cells of different densities. Orange: No cell, gray: 2.5×10^5 cells/mL, black: 5×10^5 cells/mL, red: 7.5×10^5 cells/mL, blue: 1×10^6 cells/mL, and green: 2×10^6 cells/mL. For the EIS spectra, the figure inset zooms into a small Re[Z] range displaying the impedance behavior of the cell-free SPE (orange), and the SPE seeded with 2.5×10^5 cells/mL (gray), and 5×10^5 cells/mL (black) densities. **E** EIS, **F** CV, and **G** DPV results for the SPE seeded with MCF-7 cells of 5×10^5 cells/mL density under different PTX concentrations, e.g., 1 nM (red), 5 nM (blue), and 50 nM (green) with the control group (black). Figure 4E-inset shows the equivalent circuit model used to fit the EIS data.

particularly during the G2 and M phases of the cell cycle. This interference with microtubule dynamics prevents cells from progressing through the cell cycle. Furthermore, the drug can trigger apoptosis, a programmed cell death process, leading to the elimination of damaged or abnormal cells. PTX is employed in the treatment of various cancers, including breast, ovarian, lung, and Kaposi's sarcoma[48].

For the PTX experiments, we prepared SPEs seeded with MCF-7 cells at a density of 5×10^5 cells/mL under culture medium, which were incubated in a commercial incubator for 24 h prior to drug exposure to ensure healthy morphology and attachment of cells. After this incubation period, the culture medium was replaced with the drug-containing medium with PTX at standard SOC concentrations, specifically 1, 5, and 50 nM. The cells were then incubated for an additional 24 h under these conditions for drug exposure. Our PTX study demonstrated notable alterations in EIS, CV, and DPV measurements as PTX concentration varied, highlighting the intricate interplay between PTX-induced cell death and electrochemical responses at the cell-electrode interface. As PTX has an anti-tumor effect on MCF-7 cells, high drug concentrations further decrease the number of cells adhered on the electrode surface, i.e., we observed contrasting trends compared to the scenario with increasing cell density alone. In EIS analyses (Fig. 5E), we found that impedance decreases with PTX concentration. This deviation from the usual pattern that is attributed to the cytotoxic effects of PTX on the adhered cells increases with PTX concentration, and induces cell death, resulting in reduced cell coverage on the electrode surface. Consequently, the available area for electrochemical reactions expands, facilitating enhanced mobility of charge carriers and thus decreasing impedance. Here, the Rct values determined for the control group (black curve, 2245 Ω) gradually decrease with PTX concentration, e.g., 1735 Ω for 1 nM (red curve), 1384 Ω for 5 nM (blue curve), and 1002 Ω for 50 nM (green curve).

Conversely, in CV analyses (Fig. 5F), we observed an increase in the peak current signal for higher PTX concentration. Increasing the impact of the PTX-induced cell death on the electrode surface with PTX concentration, the number of cells adhering to the electrode surface decreases. This reduction in cell coverage leads to fewer physical obstructions for electroactive species in the solution, promoting a more efficient transfer of charge carriers between the electrode and the solution, and consequently resulting in an increase in the peak amplitude. Consequently, the anodic peak current amplitude for the control group (black curve, 13.4 μA) increases with PTX

concentration, e.g., 14 μA for 1 nM (red curve), 17.1 μA for 5 nM (blue curve), and 20.9 μA for 50 nM (green curve). Similarly, in DPV, we noted an elevation in peak current signals with higher PTX concentrations, which is attributed to the diminished hindrance to electroactive species accessibility caused by PTX-induced cell death. As PTX concentration increases, the formation of a sparser cell layer on the electrode surface allows for greater access of electroactive species to the electrode. Consequently, more electroactive species are available for redox reactions, leading to an increase in the peak current signals. Here, the peak current amplitude for the control group (black curve, 3.8 μA) increases for higher PTX concentrations, e.g., 5.2 μA for 1 nM (red curve), 7.8 μA for 5 nM (blue curve), and 26.5 μA for 50 nM (green curve). Moreover, the decrease in cell coverage induced by higher PTX concentrations may contribute to a reduction in charge transfer resistance at the electrode-electrolyte interface. This decrease in resistance facilitates a more efficient transfer of charge carriers, such as electrons or ions, between the electrode and the solution, potentially leading to an increase in peak current signals. In summary, our results demonstrate that we can evaluate the anti-tumor effect of SOC drugs on cancer cells using our electrochemical analysis platform.

Discussion

In conclusion, the development of our incubator-integrated electrochemical analysis platform brings a significant advancement in cell-based electrochemical analysis, offering high precision in the study of complex biological systems. By addressing the challenge of maintaining experimental fidelity to in-vivo cellular environments, our platform provides a transition for live cells from culture to analysis while preserving their physiological conditions. Through the integration of the microfluidic, incubator, and measurement modules, our platform facilitates intimate interactions between cells and electrodes, enabling precise electrochemical measurements with independent control over culture and measurement environments. Additionally, the developed sample preparation apparatus mitigates surface degradation of electrodes during incubation, ensuring robust cell adhesion and reliable experimental outcomes. Our comprehensive studies on MCF-7 cells demonstrate the platform's efficacy and versatility in distinguishing different cell densities, critical for investigations into cell proliferation dynamics over time. Furthermore, our platform's ability to assess the anti-tumor effects of a SOC drug demonstrates its potential for evaluating drug efficacy through electrochemical methodologies. Overall, the developed incubator-integrated electrochemical analysis platform holds a significant prospect in cellular analyses and therapeutic developments, which could be critical for advanced biomedical research.

Materials

Cell culture procedure

For electrochemical analyses, we used MCF-7, which is an adherent breast-cancer cell line. Cells were cultured and maintained in 75 cm^2 flasks containing RPMI 1640 medium (Sigma-Aldrich®) with 10% fetal bovine serum (Sigma-Aldrich®), penicillin (100 units/mL, Sigma-Aldrich®), and streptomycin (100 μg/mL, Sigma-Aldrich®) at 37 °C in a humidified incubator containing 5% CO_2. All reagents were of analytical grade and directly used for the experiments as supplied. Ultrapure water (resistivity ≥18 MΩ·cm) prepared with a water purification system (Millipore) was used in all assays and solutions. Cells were detached from the flask surface by trypsinization (trypsin obtained from Sigma-Aldrich®) after reaching 80% confluency and suspended in a fresh medium. Phosphate buffer saline (PBS with pH 7.4, Sigma-Aldrich®) was used for rinsing during the cell suspension process.

Electrochemical measurements

For the electrochemical measurements, we used screen-printed carbon electrodes (Metrohm DropSens), and PalmSens4 (PalmSens®) handheld analyzer. Preventing contamination or impurities on SPE surfaces enhances the stability, sensitivity, electrode lifespan, and overall reliability of electrochemical measurements. Thus, each fresh SPE was pre-treated using DPV to remove production-related impurities from their surfaces. For the pre-treatment step, we performed an optimization study by applying potential values between +1.2 and +1.9 V for varying durations under 100 μL of acetate buffer (ACB), which yields an optimum condition of +1.8 V potential applied for a period of 60 s. The 0.5 M acetate buffer (pH: 4.8) contains 20 mM sodium chloride.

Before each measurement, the electrode surface was gently washed with 1× PBS buffer solution (pH 7.4). In EIS measurements, resistance responses obtained at varying frequency points were recorded by applying an AC amplitude of 10 mV in the frequency range of 0.1 Hz to 100 kHz. In CV analyses, current responses were recorded for the applied potential in the range between −0.6 and +0.6 V at a scan rate of 50 mV/s, while the DPV measurements were carried out in the range between −0.4 and +0.8 V at 50 mV/s scan rate. After activation, SPEs were placed in the sample preparation apparatus, and cells were seeded on the SPE surface, followed by overnight incubation in a commercial incubator under 37 °C, 5% CO_2, and 95% humidity. After incubation, the cell medium was aspirated from the electrode surface, and SPE was washed with 1× PBS (pH 7.4). Finally, electrochemical measurements were performed using an electrochemical active redox reaction of 10 mM $K_4[Fe(CN)_6]/K_3[Fe(CN)_6]$ in 0.1 M KCl. $K_4[Fe(CN)_6]/K_3[Fe(CN)_6]$ solution serves as a stable and well-defined redox couple, which is ideal for studying fast electron transfer kinetics and electrode processes in electrochemical experiments. The chemicals used in the measurements, e.g., potassium ferricyanide ($K_3[Fe(CN)_6]$), potassium ferrocyanide ($K_4[Fe(CN)_6]$, and potassium chloride (KCl) (≥99%) were supplied from Sigma-Aldrich®.

Drug preparation and PTX experiments

PTX was supplied from Selleck Chemicals, Houston, TX, USA. The stock solution of PTX was prepared by dissolving the PTX in anhydrous dimethyl sulfoxide (DMSO) at the concentration of 50 mM, and diluted with a culture medium. After activation, MCF-7 samples with 5×10^5 cells/mL density were seeded on the SPE surface under culture medium, and placed inside a commercial incubator overnight. After adhesion, the culture medium was replaced with the one containing PTX, and cells were treated with different PTX concentrations for 24 h. The drug medium was then aspirated from the electrode surface, and SPEs were washed with 1× PBS (pH 7.4). Finally, electrochemical measurements were performed in 10 mM $K_4[Fe(CN)_6]/K_3[Fe(CN)_6]$ in 0.1 M KCl solution.

Scanning electron microscopy

Scanning electron microscopy (SEM, Zeiss) was employed to examine the morphological structure of cells seeded on SPEs. Initially, cells were seeded at a density of 0.5×10^4 cells/mL, and incubated for 24 h at 37 °C in a 5% CO_2 humidified incubator. Following the incubation, the media was removed, and the SPE surface was rinsed with 1× PBS (pH 7.4). Subsequently, the cells were fixed with 2.5% glutaraldehyde (Sigma-Aldrich®) for 1 h at room temperature, followed by a PBS and distilled water wash, and dehydration was carried out with graded absolute ethanol (35, 60, 80, 90, and 100%). Samples were treated with a drying agent, e.g., HMDS/Ethanol (1:1) (Hexamethyldisilazane, Sigma-Aldrich®), and left for air-drying. After dehydration, the SPE surface was coated with gold nanoparticles using a sputter coater before SEM examination. The SEM images were captured at 8000 magnification, 20 mm working distance, and 15 kV electron high tension.

Confocal microscopy

Confocal Microscopy (Zeiss) was used to visualize stained nuclei and actin filaments of cells seeded on the SPE surface. MCF-7 cells were initially seeded at a density of 2.5×10^5 cells/mL, and incubated for 24 h at 37 °C and 5% CO_2 humidified incubator. After incubation, the SPE surface was washed with 1× PBS (pH 7.4). Cells were fixed in 4% paraformaldehyde (PFA, Sigma-Aldrich®) at room temperature, and washed with 1× PBS (pH 7.4) afterwards. Subsequently, cells were permeabilized with 0.1% Triton X-100 (Sigma-Aldrich®). They were then incubated in phalloidin (Emission Wavelength: 560 nm, Thermo Fisher Scientific Inc.) in the dark. Afterward,

a DAPI (Emission Wavelength: 457 nm, Thermo Fisher Scientific Inc.) working solution was added and incubated at room temperature. The samples were washed with 1× PBS (pH 7.4) afterward. In confocal microscopy, an excitation wavelength of 543 nm was used for phalloidin (actin staining), and 405 nm was used for DAPI (nucleus staining).

Data availability

The raw data files supporting this study are available from the corresponding author upon reasonable request.

Received: 22 October 2024; Accepted: 16 January 2025;
Published online: 31 January 2025

References

1. Wu, Y. et al. Simultaneous and sensitive determination of ascorbic acid, dopamine and uric acid via an electrochemical sensor based on PVP-graphene composite. *J. Nanobiotechnol.* **18**, 112 (2020).
2. Wang, J. Electrochemical biosensors: towards point-of-care cancer diagnostics. *Biosens. Bioelectron.* **21**, 1887–1892 (2006).
3. Maduraiveeran, G., Sasidharan, M. & Ganesan, V. Electrochemical sensor and biosensor platforms based on advanced nanomaterials for biological and biomedical applications. *Biosens. Bioelectron.* **103**, 113–129 (2018).
4. Wang, X. et al. Electrochemical signal amplification strategies and their use in olfactory and taste evaluation. *Biosensors* **12**, 566 (2022).
5. Minteer, S. D. Advances in electroanalytical chemistry. *J. Am. Chem. Soc.* **140**, 2701–2703 (2018).
6. Wu, J., Liu, H., Chen, W., Ma, B. & Ju, H. Device integration of electrochemical biosensors. *Nat. Rev. Bioeng.* **1**, 346–360 (2023).
7. Liang, G. et al. Development of the screen-printed electrodes: a mini review on the application for pesticide detection. *Environ. Technol. Innov.* **28**, 102922 (2022).
8. Hayat, A., Haider, W., Rolland, M. & Marty, J.-L. Electrochemical grafting of long spacer arms of hexamethyldiamine on a screen printed carbon electrode surface: application in target induced ochratoxin A electrochemical aptasensor. *Analyst* **138**, 2951 (2013).
9. Aflatoonian, M. R. et al. A screen-printed electrode modified with graphene/CO_3O_4 nanocomposite for electrochemical detection of tramadol. *Front. Chem.* **8**, 562308 (2020).
10. Li, M., Li, D.-W., Xiu, G. & Long, Y.-T. Applications of screen-printed electrodes in current environmental analysis. *Curr. Opin. Electrochem.* **3**, 137–143 (2017).
11. Ahamed, A. et al. Environmental footprint of voltammetric sensors based on screen-printed electrodes: an assessment towards "green" sensor manufacturing. *Chemosphere* **278**, 130462 (2021).
12. Medina-Plaza, C. et al. The advantages of disposable screen-printed biosensors in a bioelectronic tongue for the analysis of grapes. *LWT Food Sci. Technol.* **62**, 940–947 (2015).
13. Inam, A. K. M. S. et al. Flexible screen-printed electrochemical sensors functionalized with electrodeposited copper for nitrate detection in water. *ACS Omega* **6**, 33523–33532 (2021).
14. Dou, J. et al. A screen-printed, amperometric biosensor for the determination of organophosphorus pesticides in water samples. *J. Environ. Sci.* **24**, 956–962 (2012).
15. Wang, D. et al. Efficient separation and quantitative detection of Listeria monocytogenes based on screen-printed interdigitated electrode, urease and magnetic nanoparticles. *Food Control* **73**, 555–561 (2017).
16. Mahmoudi-Moghaddam, H., Tajik, S. & Beitollahi, H. Highly sensitive electrochemical sensor based on La3+-doped Co3O4 nanocubes for determination of sudan I content in food samples. *Food Chem.* **286**, 191–196 (2019).
17. Nicholas, P., Pittson, R. & Hart, J. P. Development of a simple, low cost chronoamperometric assay for fructose based on a commercial graphite-nanoparticle modified screen-printed carbon electrode. *Food Chem.* **241**, 122–126 (2018).
18. Martín-Yerga, D. & Costa-García, A. Towards a blocking-free electrochemical immunosensing strategy for anti-transglutaminase antibodies using screen-printed electrodes. *Bioelectrochemistry* **105**, 88–94 (2015).
19. Saxena, K., Chauhan, N., Malhotra, B. D. & Jain, U. A molecularly imprinted polymer-based electrochemical biosensor for detection of VacA virulence factor of H. pylori causing gastric cancer. *Process Biochem.* **130**, 87–95 (2023).
20. Radi, A.-E., Khafagy, A., El-shobaky, A. & El-mezayen, H. Anodic voltammetric determination of gemifloxacin using screen-printed carbon electrode. *J. Pharm. Anal.* **3**, 132–136 (2013).
21. García-Miranda Ferrari, A., Rowley-Neale, S. J. & Banks, C. E. Screen-printed electrodes: transitioning the laboratory in-to-the field. *Talanta Open* **3**, 100032 (2021).
22. Rojas, D. et al. Electrodeposited Prussian Blue on carbon black modified disposable electrodes for direct enzyme-free H_2O_2 sensing in a Parkinson's disease in vitro model. *Sens. Actuat. B Chem.* **275**, 402–408 (2018).
23. Hannah, S. et al. Rapid antibiotic susceptibility testing using low-cost, commercially available screen-printed electrodes. *Biosens. Bioelectron.* **145**, 111696 (2019).
24. Abdelaziz, M. H., El Sawy, E. N. & Abdelnaser, A. A novel electrochemical differentiation between exosomal-RNA of breast cancer MCF7 and MCF7/ADR-resistant cells. *Pharmaceuticals* **16**, 540 (2023).
25. Damiati, S. et al. Embedded disposable functionalized electrochemical biosensor with a 3D-printed flow cell for detection of hepatic oval cells (HOCs). *Genes* **9**, 89 (2018).
26. Ding, L., Du, D., Wu, J. & Ju, H. A disposable impedance sensor for electrochemical study and monitoring of adhesion and proliferation of K562 leukaemia cells. *Electrochem. Commun.* **9**, 953–958 (2007).
27. Guohua, H., Hongyang, L., Zhiming, J., Danhua, Z. & Haifang, W. Study of small-cell lung cancer cell-based sensor and its applications in chemotherapy effects rapid evaluation for anticancer drugs. *Biosens. Bioelectron.* **97**, 184–195 (2017).
28. ÇETİN, A. E. A portable and low-cost incubator system enabling real-time cell imaging based on a smartphone. *Turkish J. Phys.* **47**, 279–296 (2023).
29. Tayebi-khorami, M. et al. Construction a CO2 incubator for cell culture with capability of transmitting microwave radiation. *J. Med. Signals Sensors* **12**, 127 (2022).
30. Walzik, M. P. et al. A portable low-cost long-term live-cell imaging platform for biomedical research and education. *Biosens. Bioelectron.* **64**, 639–649 (2015).
31. Johnson, M. A. in *PID Control*. 1–46 (Springer-Verlag).
32. Juanole, G., Mouney, G., Calmettes, C. & Peca, M. in *Fieldbus Systems and Their Applications 2005*. 79–86 (Elsevier, 2006).
33. Ellis, G. in *Control System Design Guide* 97–119 (Elsevier, 2012).
34. Randviir, E. P. & Banks, C. E. A review of electrochemical impedance spectroscopy for bioanalytical sensors. *Anal. Methods* **14**, 4602–4624 (2022).
35. Wang, S. et al. Electrochemical impedance spectroscopy. *Nat. Rev. Methods Prim.* **1**, 41 (2021).
36. Magar, H. S., Hassan, R. Y. A. & Mulchandani, A. Electrochemical impedance spectroscopy (EIS): principles, construction, and biosensing applications. *Sensors* **21**, 6578 (2021).
37. Lazanas, A. C. & Prodromidis, M. I. Electrochemical impedance spectroscopy—a tutorial. *ACS Meas. Sci. Au.* **3**, 162–193 (2023).
38. Climent, V. & Feliu, J. M. C. in *Encyclopedia of Interfacial Chemistry.* 48–74 (Elsevier, 2018).
39. Elgrishi, N. et al. A practical beginner's guide to cyclic voltammetry. *J. Chem. Educ.* **95**, 197–206 (2018).

40. Liu, J. et al. Application and progress of chemometrics in voltammetric biosensing. *Biosensors* **12**, 494 (2022).
41. Liu, J. et al. Salivary cortisol determination on smartphone-based differential pulse voltammetry system. *Sensors* **20**, 1422 (2020).
42. Venton, B. J. & DiScenza, D. J. in *Electrochemistry for Bioanalysis.* 27–50 (Elsevier, 2020).
43. Lebaron, R. G. & Athanasiou, K. A. Ex vivo synthesis of articular cartilage. *Biomaterials* **21**, 2575–2587 (2000).
44. Sousa-Pimenta, M. et al. Chemotherapeutic properties and side-effects associated with the clinical practice of terpene alkaloids: paclitaxel, docetaxel, and cabazitaxel. *Front. Pharmacol.* **14**, 1157306 (2023).
45. Abu Samaan, T. M., Samec, M., Liskova, A., Kubatka, P. & Büsselberg, D. Paclitaxel's mechanistic and clinical effects on breast cancer. *Biomolecules* **9**, 789 (2019).
46. Refolo, M. G., Lotesoriere, C., Lolli, I. R., Messa, C. & D'Alessandro, R. Molecular mechanisms of synergistic action of Ramucirumab and paclitaxel in gastric cancers cell lines. *Sci. Rep.* **10**, 7162 (2020).
47. Delavari, B. et al. A biophysical study on the mechanism of interactions of DOX or PTX with α-lactalbumin as a delivery carrier. *Sci. Rep.* **8**, 17345 (2018).
48. Mustafa, G. et al. Nanoscale drug delivery systems for cancer therapy using paclitaxel—a review of challenges and latest progressions. *J. Drug Deliv. Sci. Technol.* **84**, 104494 (2023).

Acknowledgements

A.E.C. acknowledges The Scientific and Technological Research Council of Türkiye (TÜBİTAK) (Project No. 122E384).

Author contributions

A.E.C. served as the principal investigator, providing supervision and securing funding for the project. S.N.T. and A.E.C. conceptualized the idea. F.K., M.B.A., H.B.A., and A.E.C. developed the system hardware. F.K. and S.N.T. conducted the electrochemical experiments. F.K. performed the cell culture procedures. M.B.A. and H.B.A. designed the system software. All authors contributed to the preparation of the manuscript.

Competing interests

S.N.T. and A.E.C. have a pending patent application for the technology presented in this paper. All other authors declare no competing interests.

Additional information

Supplementary information The online version contains supplementary material available at https://doi.org/10.1038/s44328-025-00030-5.

Correspondence and requests for materials should be addressed to Arif E. Cetin.